

Photopyroelectric thermal-wave tomography of aluminum with ray-optic reconstruction

Mahendra Munidasa and Andreas Mandelis

Photoacoustic and Photothermal Sciences Laboratory, Ontario Laser and Lightwave Research Centre, Department of Mechanical Engineering, University of Toronto, Toronto, Ontario M5S 1A4, Canada

Received August 27, 1990; revised manuscript received June 24, 1991; accepted June 24, 1991

A capacitive photopyroelectric tomographic technique for obtaining spatial and depth-resolved photothermal scanning images of opaque solid samples is reported. Unlike the two-dimensional projection images obtained by conventional photothermal detection methods, tomographic reconstruction for depth-resolved imaging of subsurface defects is demonstrated to be possible with the assumption of raylike propagation of thermal waves.

INTRODUCTION

Thermal-wave imaging has emerged as a useful technique for nondestructive evaluation of subsurface features in opaque solids.¹ This method has advantages, especially in near-surface defect detection with a variable depth range, compared with conventional techniques such as ultrasonic and x-ray inspection. In thermal-wave imaging a (laser or electron) beam of energy, modulated at a certain frequency, is focused and scans across the sample surface. The resulting periodic heat flow in the material is a diffusive process, producing a periodic temperature distribution that is called a thermal wave. These waves will reflect and scatter from features beneath the surface that have different thermal characteristics from their surroundings. Several different detection methods²⁻⁵ have been used to detect these thermal waves. Each method has its own advantages and disadvantages.

Recently thin-film pyroelectric detection has emerged as a convenient and inexpensive method of thermal-wave imaging.⁶ Pyroelectric detection instrumentation^{7,8} that is capable of sampling the local thermal-wave field value in the back of a sample has been developed. This permits spatially resolved scans⁹ of this field, in contrast to the spatially integrated detection mode of earlier investigations.⁶ Images obtained by the methods reported previously are two-dimensional projections of subsurface features. These images are projections in the sense that the image is formed by mapping the surface ac temperature that is due to the forward (back-surface detection) or backward (front-surface detection) scattered thermal waves in a two-dimensional raster without regard to the actual depth of scatterers. Although research has been done toward obtaining depth-resolved information on subsurface features by using equivalent experimental techniques^{10,11} and depth profiling of layered samples,¹²⁻¹⁴ no research has been reported toward obtaining tomographic images by using thermal waves. The transmission radiometric method of Busse and Renk¹⁰ also permits the performance of tomographic scans like those from our pyroelectric detection instrumentation; however, this ability has not been tomographically implemented so far. Since the pyroelectric detector senses the sample back-surface

temperature directly, it needs a very low incident laser power (10 mW is adequate below 30 Hz for an aluminum sample that is 2 mm thick) compared with a power of several watts needed in radiometric measurements, which are limited by the small value of the Stefan-Boltzmann constant. A photothermal method based on the mirage effect was used to obtain depth information on the presence of defects by means of a tomographiclike procedure¹¹; this method was limited by the line-integral nature of the probe beam to point-by-point reconstruction of projectional images on correlations of angular scans. This technique, however, cannot yield tomographic imaging of cross-sectional planes in materials because of the line-integral nature of the probe beam.

Tomography refers to cross-sectional imaging of an object on reconstruction from its projections from different directions. A projection at a given angle is the average (e.g., the line integral of the absorption coefficient in the case of x-ray tomography) of a material in the direction specified by that angle. The consequence of this technique for x-ray, ultrasound, radioisotope, and magnetic resonance imaging in medical diagnostics has been revolutionary. It has also been used in geophysical surveys¹⁵ and nondestructive testing.¹⁶

We report here, for the first time to our knowledge, the preliminary investigation performed toward reconstructing a thermal-wave tomographic image with a synthetic aperture approach and the pyroelectric detection instrumentation mentioned above.^{7,8} Raylike propagation^{17,18} of thermal waves is assumed in order to demonstrate the possibility of thermal-wave tomography. The validity of this approximation is discussed with regard to experimental data.

EXPERIMENTAL METHOD AND DATA

The instrumentation used here is a new capacitively coupled pyroelectric detection instrument reported previously.⁷ This instrumentation involves a polyvinylidene fluoride (PVDF) thin pyroelectric film attached to the back of the sample and a remote-metal-tip detection geometry. For spatially resolved measurements the back-surface electrode of the film is replaced with a metal pin

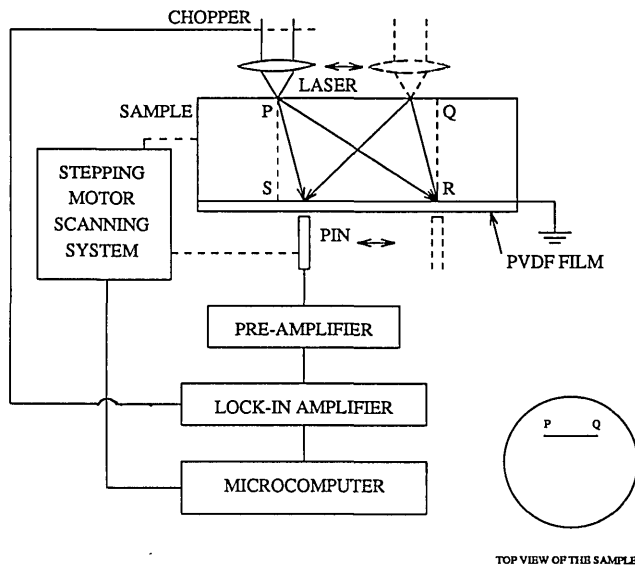


Fig. 1. Cross section (*PQRS*) to be imaged, showing the lines joining two laser-pin scanning positions and the detection electronics. The insert shows the top view of the sample with scan line *PQ*.

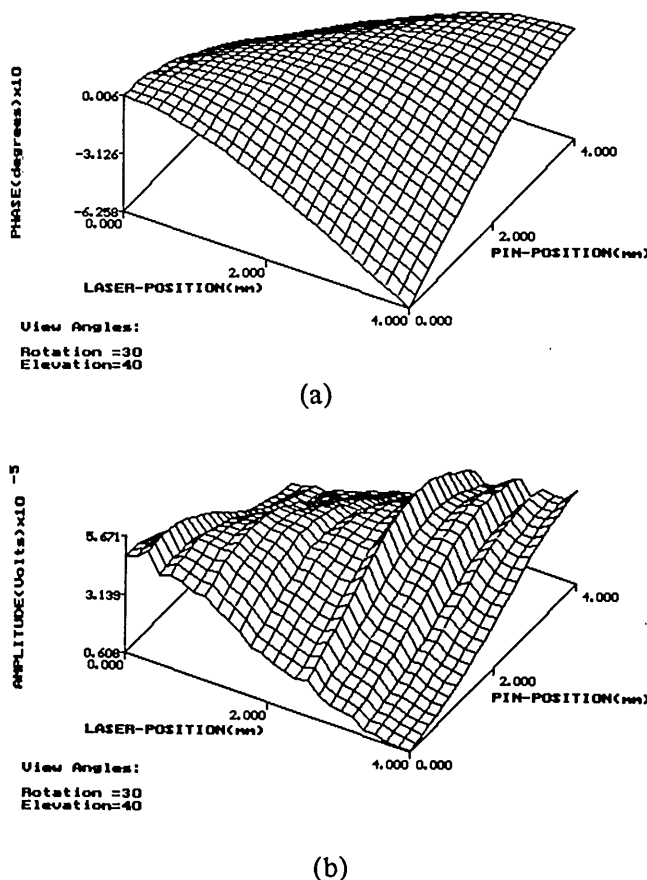


Fig. 2. (a) Phase and (b) amplitude data with a modulation frequency of 16 Hz, obtained from a tomographic scan along a straight line of length 4 mm, defining a cross section of a defect-free aluminum sample of thickness 2 mm. The distance between two data points is 0.16 mm. In this and the figures below the view angle definitions are as follows: rotation, the angle between the pin position (or *y*) axis and the line of sight (when the elevation angle is 0°); elevation, the angle between the coordinate plane (or *x-y*) and the line of sight. Angles are expressed in degrees.

of diameter 0.8 mm in order to sample the local ac electric field, which is proportional to the ac temperature field generated by the modulated laser beam (from a 1.2-W Nd:YAG laser at 1.06 μm) focused onto the front surface of the sample. Locating the pin away from the PVDF film allows one to scan the pin over the back surface of the sample to obtain the local ac temperature distribution. Since both the modulated heating source and the detector are localized and can be scanned independently, it is possible to perform a limited-angle tomographic scan with this instrument. The signal is synchronously detected by a lock-in amplifier. The sample and the pin are mounted on separate micrometer stages that are attached to stepping motors. The data are collected by a microcomputer, which also controls the stepping motors. Typical data collection time for a 25×25 -point scan with a 1-s time constant is ~ 2 h.

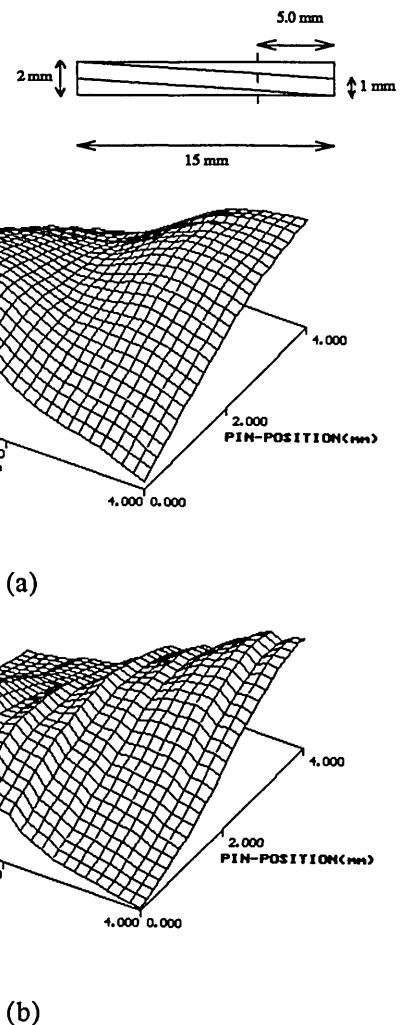


Fig. 3. (a) Phase and (b) amplitude data with a modulation frequency of 16 Hz, obtained from a tomographic scan along a straight line of length 4 mm, defining a cross section with a 1-mm-diameter hole close to the back surface (the center of the hole is 1.2 mm deep) in an aluminum sample of thickness 2 mm. The distance between two data points is 0.16 mm. The inset in (a) shows the cross section along the length of the hole, with the dashed line indicating the cross section to be imaged and with the scanning laser on top. The scan line is perpendicular to the page.

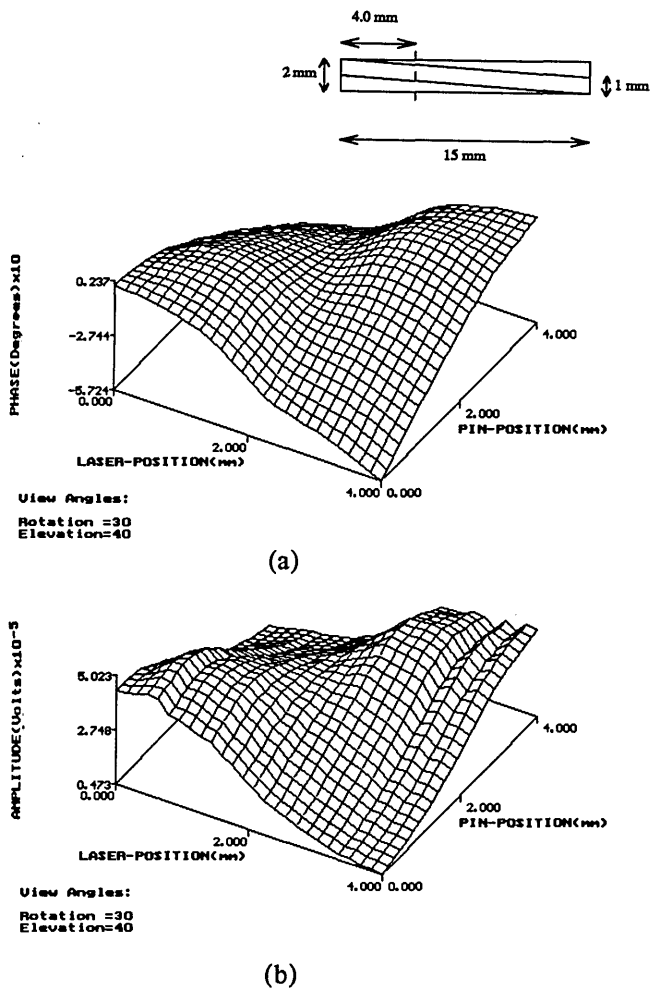


Fig. 4. (a) Phase and (b) amplitude data with a modulation frequency of 16 Hz, obtained from a tomographic scan along a straight line of length 4 mm, defining a cross section with a 1-mm-diameter hole close to the front surface (the center of the hole is 0.8 mm below the surface) in an aluminum sample of thickness 2 mm. The distance between two data points is 0.16 mm. The inset in (a) shows the cross section along the length of the hole, with the dashed line indicating the cross section to be imaged (perpendicular to the page) and with the scanning laser on top.

Circular aluminum samples of thickness 2 mm and diameter 15 mm with various subsurface defects were used in this experiment.

Scans across cross sections to be imaged are performed as shown in Fig. 1. For each laser position data were collected at several pin positions along a straight line PQ (Fig. 1 insert), which define the cross-sectional plane ($PQRS$ of Fig. 1) to be imaged. Phase and amplitude data (laser-pin position versus signal) obtained from such a tomographic scan across a cross section of a uniform aluminum sample are shown in Fig. 2 [e.g., laser position Q and pin position S in Fig. 1 refer to the coordinate (4 mm, 0 mm) in Figs. 2(a) and 2(b)]. Tomographic scans taken along several cross sections (as indicated by a vertical dashed line in each figure insert below) of samples with slanted holes drilled through the center (diameter) of the disk are shown in Figs. 3–6. Figures 3 and 4 show phase and amplitude data taken with a modulation frequency of 16 Hz across two cross sections 6 mm apart

over a slanted hole of diameter 1 mm. The insets in Figs. 3(a) and 4(a) show the details of the positions of each cross section (the scan line is perpendicular to the page). Similar scans over a slanted hole of diameter 0.5 mm taken at 16 and 80 Hz are shown in Figs. 5 and 6, respectively. The effect of the change in hole size can be clearly seen by comparing the data of Figs. 4 and 5. Figures 2–5 show that photothermal amplitude data are dominated by the inhomogeneities in the surface reflectance. The line structure seen in the amplitude data of these samples is due to the machining lines on the surface. The absence of these lines from the phase data clearly shows that this response is purely a change in surface absorption. These features result in a deterioration in the signal-to-noise ratio of the scan to the point of sometimes concealing the information from small subsurface defects (e.g., a 0.5-mm hole). On the contrary, the photopyroelectric phase yields true thermal-wave scattering, independent of the surface reflectance, a feature that is common to all photothermal

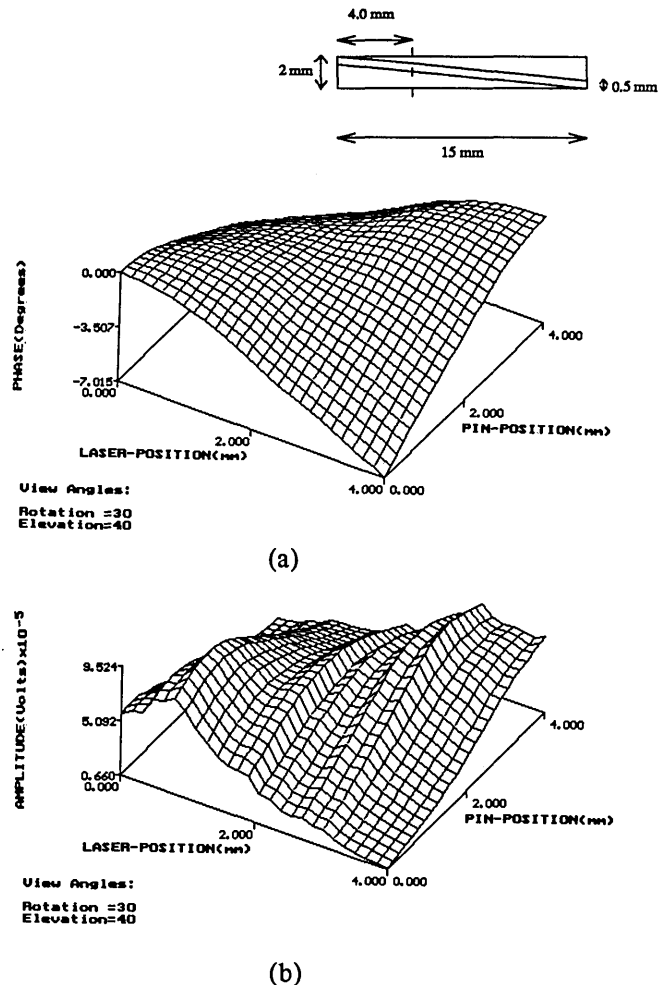
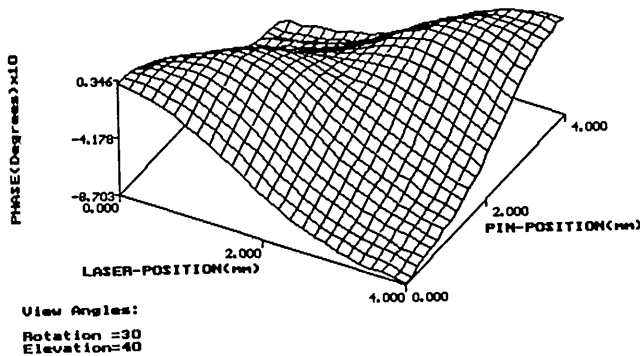
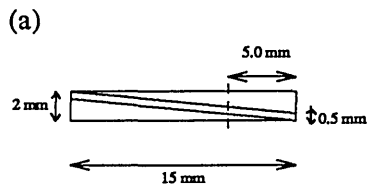
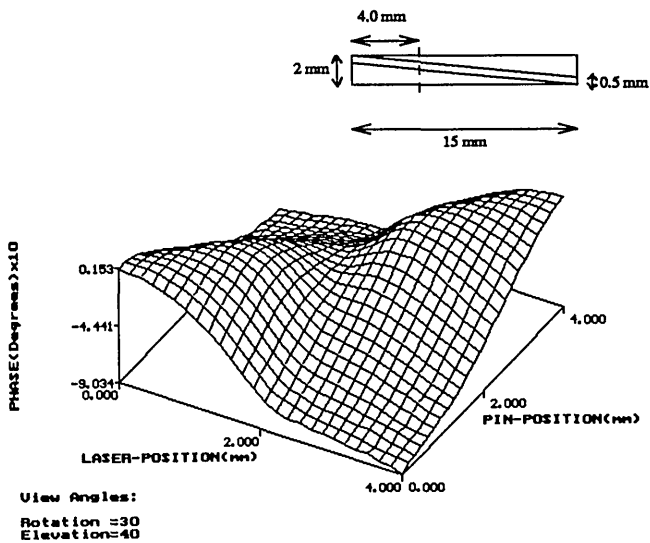


Fig. 5. (a) Phase and (b) amplitude data with a modulation frequency of 16 Hz, obtained from a tomographic scan along a straight line of length 4 mm, defining a cross section with a 0.5-mm-diameter hole close to the front surface (the center of the hole is 0.65 mm below the surface) in an aluminum sample of thickness 2 mm. The distance between two data points is 0.16 mm. The inset in (a) shows the cross section along the length of the hole, with the dashed line indicating the cross section to be imaged (perpendicular to the page) and with the scanning laser on top.



(b)

Fig. 6. Phase data with a modulation frequency of 80 Hz, obtained from a tomographic scan along a straight line of length 4 mm, defining a cross section with a 0.5-mm-diameter hole, where (a) the center is 0.65 mm below the surface and (b) the center is 1.25 mm below the surface in an aluminum sample of diameter 15 mm and thickness 2 mm. The distance between two data points is 0.16 mm. The insets show the cross section along the length of the hole, with the dashed line defining the cross section to be imaged (perpendicular to the page) and with the scanning laser on top.

techniques.⁴ Thus both Figs. 5(a) and 6 are seen to contain information about the subsurface structure of the chosen cross section. Another notable feature is that the phase data taken at 80 Hz [Fig. 6(a)] clearly show a better contrast than the lower-frequency (16 Hz) data [Fig. 5(a)].

Figure 7 shows a scan taken across one cross section of a fatigue crack on an aluminum sample of thickness 2 mm. The crack has propagated from the heating surface into the material. This sample was made by using the three-point bending method¹⁹ on a 3-mm-thick aluminum strip. A portion 0.5 mm wide was machined away from each side to remove any surface nonuniformities caused by bending and to eliminate any trace of the crack

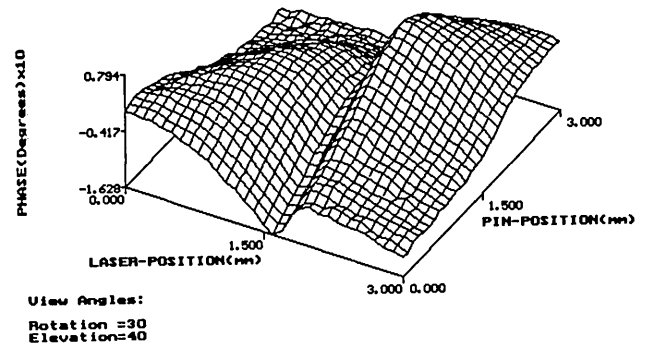
under an optical microscope. A conventional photo-thermal image (two-dimensional projection) of an area 3 mm × 3 mm of this crack, obtained by scanning the Nd:YAG laser and the pin together with the pin directly below the laser spot, is shown in Fig. 8. This type of imaging does not give any information about the depth of the crack. Tomographic scan data shown in Fig. 7 were taken across a line parallel to the x axis in Fig. 8.

RECONSTRUCTION ALGORITHM

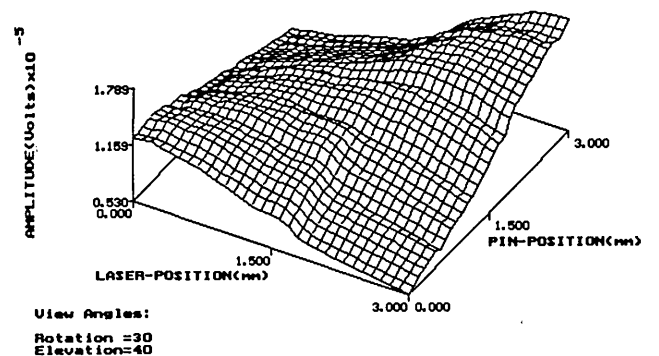
Our reconstruction method is similar to that used in x-ray tomography. In x-ray tomography the image obtained is a map of the attenuation coefficient (γ) of x rays through the medium determined for a large number of points within the cross section. The x-ray intensity is given by

$$I = I_0 \exp(-\gamma x), \tag{1}$$

where I_0 is the incident intensity and I is the intensity after a penetration distance x . The problem of determining the values of γ was first approached by imagining each cross section as divided into rectangular pixels. By measuring the total attenuation of a pencil beam of radiation passing through the material, the sum of the attenuation that is due to a particular set of these pixels is determined. Many measurements from different directions will determine the line sums for different sets of pixels.



(a)



(b)

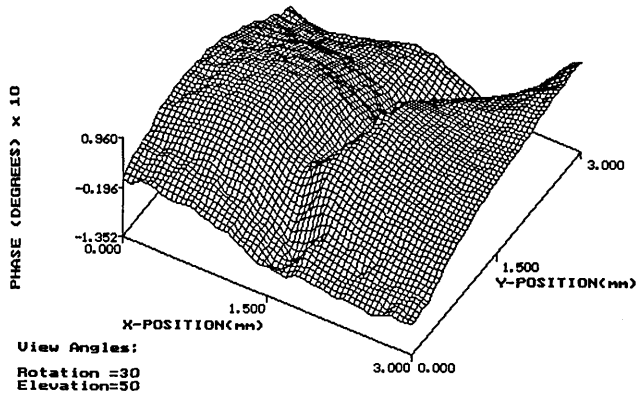
Fig. 7. (a) Phase and (b) amplitude data with a modulation frequency of 150 Hz, obtained from a tomographic scan along a straight line of length 3 mm, defining a cross section with a fatigue crack propagated from the front surface into the bulk in an aluminum sample of thickness 2 mm. The distance between two data points is 0.1 mm.

tance x from the heat source is given by

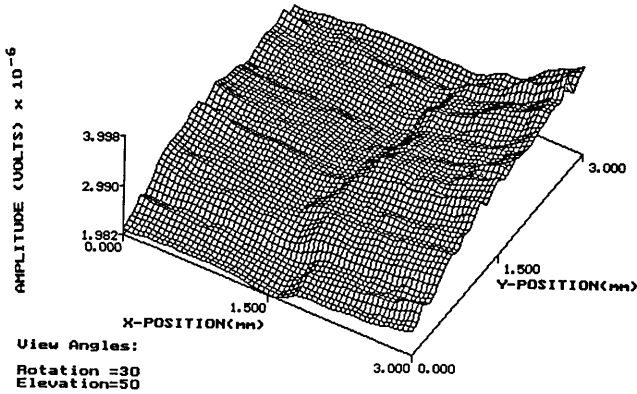
$$A = A_0 \exp(-x/\mu), \quad (3)$$

$$P = -(x/\mu) + \phi_0, \quad (4)$$

respectively, where μ is the thermal diffusion length, ω is the modulation angular frequency, A_0 is proportional to T_0 , the temperature at the surface, and depends on surface reflectivity, and ϕ_0 is a reference value given by the lock-in amplifier phase setting. From Eqs. (3) and (4) and experimentally obtained values for A and P , the average value of μ along the lines joining the heated spot and the



(a)



(b)

Fig. 8. (a) Phase and (b) amplitude images of a two-dimensional projection of the fatigue crack described in Fig. 7, obtained by scanning the laser (modulated at 30 Hz) and the pin together, with the pin directly below the laser spot. The distance between two data points is 0.1 mm. Data have been interpolated once for the plot. Here the x - y coordinate plane is parallel to the sample surface.

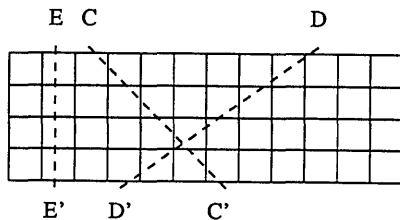


Fig. 9. Cross section of the sample to be imaged, divided into rectangular pixels. Here the thickness is divided into four rows and the number of laser positions is assumed to be 12. Lines such as CC' or EE' define the straight-line paths through which thermal waves are assumed to propagate.

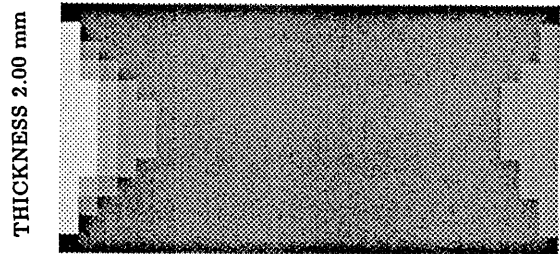
If a sufficiently large number of measurements are made, an average value for each individual pixel can be estimated. The results are mapped as shades of gray at each pixel to form an image.

A similar method is used here (Fig. 9) to reconstruct thermal-wave tomographic images. For nondiffractive propagation¹⁷ and the solution to the one-dimensional heat-flow equation given by

$$T = T_0 \exp(-x/\mu) \cos(\omega t - x/\mu), \quad (2)$$

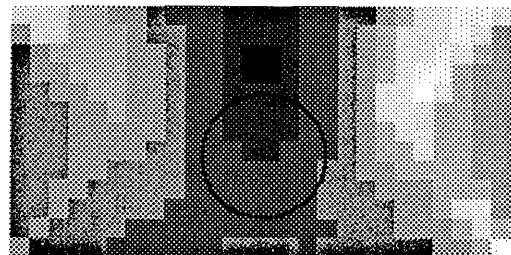
the amplitude A and the phase P of the signal at a dis-

FRONT SURFACE



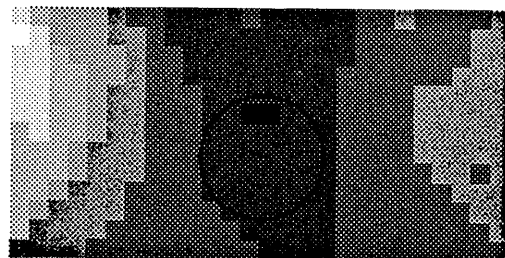
BACK SURFACE
LENGTH 4.00 mm

Fig. 10. Phase-reconstructed image from the raw data (16 Hz) of Fig. 2(a) for a uniform cross section of a 2-mm-thick aluminum sample. In this and later images darker pixels correspond to lower values of diffusivity, and the front and back surfaces are as labeled.



LENGTH 4.00 mm

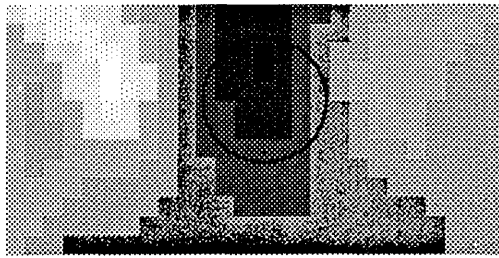
(a)



LENGTH 4.00 mm

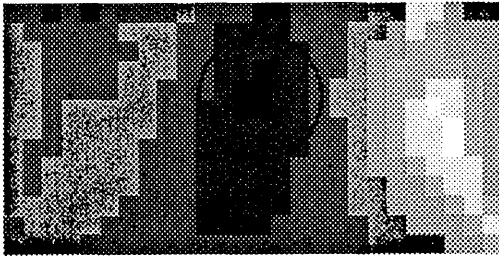
(b)

Fig. 11. (a) Phase and (b) amplitude reconstructed images from the data (16 Hz) of Fig. 3. In this and subsequent images the actual position of the hole is indicated by a circle, and the thickness (vertical length) is 2 mm.



LENGTH 4.00 mm

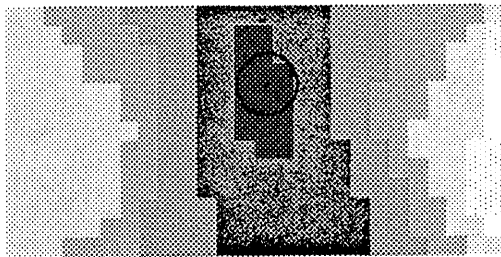
(a)



LENGTH 4.00 mm

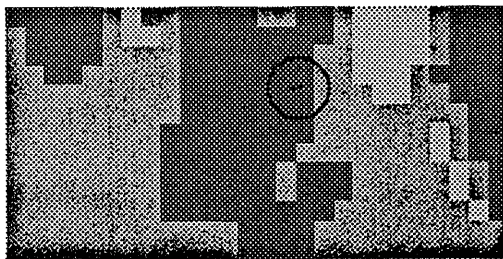
(b)

Fig. 12. (a) Phase and (b) amplitude, reconstructed images from the data (16 Hz) of Fig. 4.



LENGTH 4.0 mm

(a)



LENGTH 4.0 mm

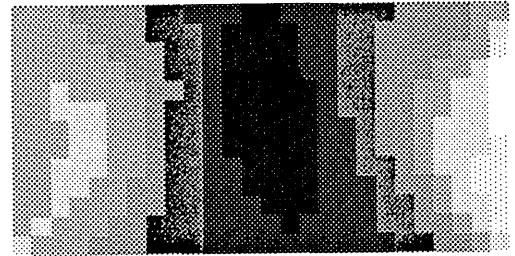
(b)

Fig. 13. (a) Phase and (b) amplitude, reconstructed images, normalized to the same gray level as in Fig. 12, from the data (16 Hz) of Fig. 5.

pin can be calculated. To eliminate the constants A_0 and ϕ_0 from the equations, assuming defect-free edges, we used data from the vertical rays at the edges of the cross section. Thermal diffusivity α , given by

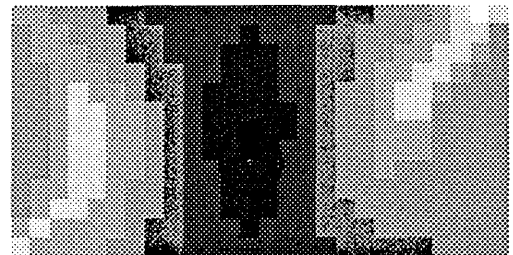
$$\alpha = \omega\mu^2/2, \tag{5}$$

is the imaged quantity. By averaging over each line, we calculate values of α for each individual pixel. The value of α for each pixel is weighted by the distance a ray travels across that particular pixel.



LENGTH 4.00 mm

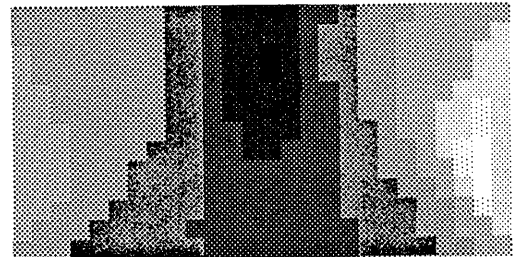
(a)



LENGTH 4.00 mm

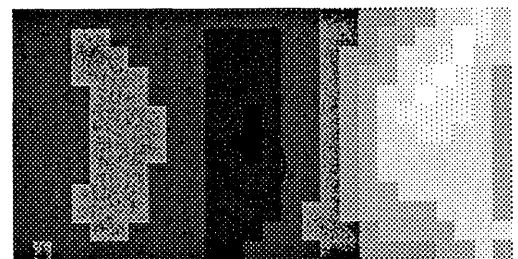
(b)

Fig. 14. Phase-reconstructed images (16 Hz) of a cross section with a 0.5-mm-diameter hole (a) close to the front surface (centered at 0.65 mm below the surface) and (b) close to the back surface (centered at 1.25 mm below the surface).



LENGTH 4.00 mm

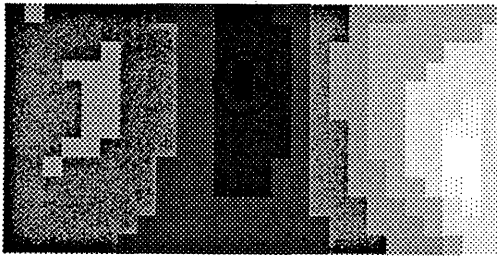
(a)



LENGTH 4.00 mm

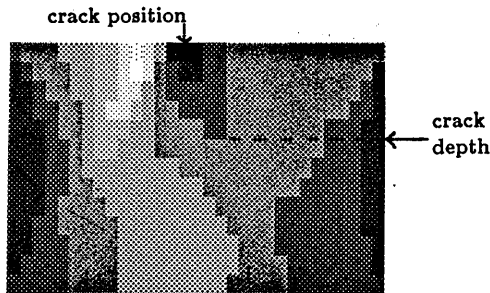
(b)

Fig. 15. Phase-reconstructed images (80 Hz) of a cross section with a 0.5-mm-diameter hole (a) centered at 0.65 mm below the surface and (b) centered at 1.25 mm below the surface.



LENGTH 4.00 mm

Fig. 16. Phase-reconstructed image (80 Hz) of a cross section [Fig. 15(a)] with a 0.5-mm-diameter hole centered at 0.65 mm below the surface, obtained by averaging the two images reconstructed from the data collected from both sides of the sample (180° rotation).



LENGTH 3.00 mm

Fig. 17. Phase-reconstructed image of the fatigue crack, obtained from the data of Fig. 7(a).

RESULTS AND DISCUSSION

Figure 10 shows the reconstructed image of the cross section, obtained from the phase data in Fig. 2(a). In all the tomograms presented below thickness is divided into 13 rows of pixels, and the number of pixels along the width is equal to the number of laser positions. Darker pixels correspond to lower values of diffusivity. The artifacts seen at the left and right edges are due to the combined effect of uneven averaging (smaller number of rays near the edge) and the failure of raylike propagation (especially for longer path lengths). This artifact is seen in all the reconstructed images shown below. The reconstruction algorithm assumes a sample of constant thickness and a fixed separation between the pin and the PVDF film along the line of scanning. Deviations from these stipulations can also lead to artifacts. Smaller photopyroelectric signals caused by greater PVDF-pin separation can be artificially interpreted by our reconstruction algorithm as sample regions of lower diffusivity. The sample with the film attached to its back was mounted on a gimbal mount and was leveled by monitoring the signal with the bare film. Data reported here were taken with a pin-film separation of 0.2 mm. Most reconstructed tomograms reported below were obtained only from cross-sectional photopyroelectric phase data for reasons discussed above.

Reconstructed images of data in Figs. 3, 4, and 5 are shown in Figs. 11, 12, and 13, respectively. In all the tomograms presented below, the actual position of the hole is indicated by a circle. Figure 14(a) shows the same cross section as Fig. 13(a) on a different gray-level scale with better contrast. Figure 14(b) shows the reconstruction of a cross section of the same sample in which the

hole (0.5 mm) is closer to the back surface at 16 Hz. Reconstructed images of data in Fig. 6 are shown in Fig. 15. Images in Figs. 11 and 12 (1-mm hole) are not normalized to the same scale as those of Figs. 14 and 15 (0.5-mm hole). The reconstructed image (Fig. 13) of the 0.5-mm hole from the raw data in Fig. 5, normalized to the scale of the 1-mm hole image (Fig. 12), shows that the effect of the size of the hole is interpreted as a change in contrast, as well as a change in size, in the crudely reconstructed image. The smaller hole is not seen in the reconstruction from amplitude data, but the surface features are clearly visible [Fig. 13(b)].

Figures 11 and 12 show that the center of the reconstructed hole cross section (based on the darkest pixel) of the 1-mm hole falls within the actual hole cross section when the hole is closer to the front surface (0.8-mm deep). Figure 12 also shows that the reconstruction from the amplitude data is more accurate in this particular case. Figure 14 shows that the position of the shallower hole [Fig. 14(a)] is more accurately reproduced than the deeper hole [Fig. 14(b)] by the reconstruction process. Comparing tomograms of the 1-mm-hole cross section with that for the 0.5-mm hole shows that the smaller feature is more accurately reproduced by this method of reconstruction. Figures 15(a) and 15(b) show results from scans at 80 Hz for the cross sections of Fig. 6(a) (inset) and 6(b) (inset), respectively. It can be seen that increasing the frequency tends to move the position of the subsurface defect toward the front surface from its actual position. This type of distortion can be eliminated by averaging the two reconstructed images that are obtained from the data collected from both sides of the sample (180° rotation), as is shown in Fig. 16. All the reconstructed images show an elongation of the hole cross section along the vertical direction. These limitations are strong indications of the need to consider a rigorous diffractive propagation²⁰ approach for thermal waves. Such an approach is currently under development and will be reported in a forthcoming paper.²¹

Finally, Fig. 17 shows the phase-reconstructed tomogram of the fatigue crack, the raw data of which are shown in Fig. 7(a). It is not possible to reconstruct the crack from the amplitude data [Fig. 7(b)]. It can be seen that the crude reconstruction correctly images the decreasing importance of the crack with depth. This may be interpreted as a decreasing extent of the crack at greater depths. From Fig. 17 it appears that the crack extends to $\sim 500 \mu\text{m}$ below the surface. The actual depth of the crack is unknown. The region with lighter pixels (higher diffusivity), seen to the left of the crack in Fig. 17, may be an artifact of the algorithm or may be a real mapping of stressed areas that are generated during the machining process; thermal-wave signals are known to be sensitive to such stressed regions.²¹

CONCLUSIONS

We have demonstrated the possibility of generating thermal-wave slice tomography by using photopyroelectric detection, mainly for the purpose of nondestructive testing. This is a new technology, complementary to x-ray and ultrasonic tomography.²² Because of the absence of multiple reflections, a unique tomographic reconstruction capability for thin materials with near-surface defect

structure can be expected. Although we have used a simple ray-optic reconstruction method, the results are encouraging and suggestive of the potential and limitations of the method as well as the importance of improved image resolution and the need for reconstruction by using the diffractive nature of thermal waves.²² With an array of pins^{23,24} data collection time can be greatly reduced.

ACKNOWLEDGMENT

We gratefully acknowledge useful discussions and the contribution to the design of the instrumentation made by Marek Mieszkowski at the early stages of this project. We also thank David Morris for his programming efforts and Leslie Sinclair for preparing the fatigue crack samples. The support of the Ontario Laser and Lightwave Research Centre is gratefully acknowledged.

REFERENCES

1. R. L. Thomas, L. D. Favro, and P. K. Kuo, "Thermal-wave imaging for nondestructive evaluation," *Can. J. Phys.* **64**, 1234-1237 (1986).
2. H. Y. Wong, R. L. Thomas, and G. F. Hawkins, "Surface and subsurface structure of solids by laser photoacoustic spectroscopy," *Appl. Phys. Lett.* **32**, 538-539 (1978).
3. M. J. Lin, L. J. Inglehart, L. D. Favro, P. K. Kuo, and R. L. Thomas, "Thermal wave detection of vertical cracks in opaque solids," *Rev. Prog. Quant. Nondestruct. Evaluat.* **4B**, 739-744 (1985).
4. G. Busse, "Optoacoustic and photothermal material inspection techniques," *Appl. Opt.* **21**, 107-110 (1982).
5. A. Rosencwaig, J. Opsal, W. L. Smith, and D. L. Willenborg, "Detection of thermal waves through optical reflectance," *Appl. Phys. Lett.* **46**, 1013-1015 (1985).
6. I. F. Faria, Jr., C. C. Ghizoni, and L. C. M. Miranda, "Photopyroelectric scanning microscopy," *Appl. Phys. Lett.* **47**, 1154-1156 (1985).
7. M. Mieszkowski, K. F. Leung, and A. Mandelis, "Photopyroelectric thermal wave detection via contactless capacitive polyvinylidene fluoride (PVDF) metal probe-tip coupling," *Rev. Sci. Instrum.* **60**, 306-316 (1989).
8. A. Mandelis and M. Mieszkowski, "Thermal wave sub-surface defect imaging and tomography apparatus," U.S. Patent 4,950,897 (August 21, 1990).
9. M. Mieszkowski and A. Mandelis, "Photopyroelectric spatially resolved imaging of thermal wave fields," *J. Opt. Soc. Am. A* **7**, 552-557 (1990).
10. G. Busse and K. F. Renk, "Stereoscopic depth analysis by thermal wave transmission for nondestructive evaluation," *Appl. Phys. Lett.* **42**, 366-368 (1983); G. Busse, "Thermal wave nondestructive depth profiling with stereoscopic photothermal detection," *J. Phys. (Paris)* **C6** (Suppl. 10), 471-474 (1983).
11. D. Fournier, F. Lepoutre, and A. C. Boccara, "Tomographic approach for photothermal imaging using the mirage effect," *J. Phys. (Paris)* **C6** (suppl. 10) 479-482 (1983).
12. H. Coufal, "Fourier analysis of frequency domain multiplexed photoacoustic signals," *J. Photoacoust.* **1**, 413-428 (1984).
13. J. Opsal and A. Rosencwaig, "Thermal-wave depth profiling: theory," *J. Appl. Phys.* **53**, 4240-4246 (1982).
14. S. B. Peralta and A. W. Williams, "Characterization of γ -Fe₂O₃ homogeneity in magnetic recording media by photoacoustics," *Appl. Phys. Lett.* **54**, 2405-2407 (1989).
15. A. J. Devaney, "Geophysical diffraction tomography," *IEEE Trans. Geosci. Remote Sensing* **GE-22**, 3-13 (1984).
16. E. Segal, W. A. Ellingson, Y. Segal, and I. Zmora, "A linearization beam hardening correction method for x-ray computed tomographic imaging of structural ceramics," *Rev. Prog. Quant. Nondestruct. Evaluat.* **6A**, 411-419 (1987).
17. J. A. Burt, "Ray theory of thermal-wave imaging," *J. Phys. (Paris)* **C6** (suppl. 10), 453-457 (1983).
18. J. A. Burt, "The thermal-wave lens," *Can. J. Phys.* **64**, 1053-1055 (1986).
19. *ASTM Book of Standards* (ASTM, Philadelphia, Pa., 1984), Vol. 03.01, p. 536.
20. A. Mandelis, "Theory of photothermal-wave diffraction and interference in condensed media," *J. Opt. Soc. Am. A* **6**, 298-308 (1989).
21. A. Mandelis, "Theory of photothermal wave diffraction tomography via spatial Laplace spectral decomposition," *J. Phys. A* **24**, 2485-2505 (1991).
22. M. Luukkala and S. G. Askerov, "Detection of plastic deformation in metals with photoacoustic microscope," *Electron. Lett.* **16**, 84-85 (1980).
23. A. C. Kak and M. Slaney, *Principles of Computerized Tomographic Imaging* (IEEE, New York, 1988), pp. 227-228.
24. R. W. Whatmore, "Pyroelectric devices and materials," *Rep. Prog. Phys.* **49**, 1335-1386 (1986).
25. R. Watton, F. W. Ainger, S. Porter, D. Pedder, and J. Gooding, "Technologies and performance for linear and two dimensional pyroelectric arrays," in *Infrared Technology X*, I. J. Spiro and R. A. Mollicone, eds., *Proc. Soc. Photo-Opt. Instrum. Eng.* **510**, 139-148 (1985).